Validity and value of metabolic connectivity in mouse models of β-amyloid and tauopathy

François Ruch [a], Johannes Gnörich [a,b], Karin Wind [a,b], Mara Köhler [a], Artem Zatcepin [a,b], Thomas Wiedemann [a], Franz-Joseph Gildehaus [a], Simon Lindner [a], Guido Boening [a], Barbara von Ungern-Sternberg [a], Leonie Beyer [a], Jochen Herms [b,c,d], Peter Bartenstein [a,b], Matthias Brendel [a,b,c,*], Florian Eckenweber [a]

[a] Department of Nuclear Medicine, University Hospital of Munich, LMU Munich, Munich, Germany
[b] German Center for Neurodegenerative Diseases (DZNE), Munich, Germany
[c] Munich Cluster for Systems Neurology (SyNergy), Munich, Germany
[d] Center of Neuropathology and Prion Research, University of Munich, Munich, Germany

ARTICLE INFO

ABSTRACT

Among functional imaging methods, metabolic connectivity (MC) is increasingly used for investigation of regional network changes to examine the pathophysiology of neurodegenerative diseases such as Alzheimer's disease (AD) or movement disorders. Hitherto, MC was mostly used in clinical studies, but only a few studies demonstrated the usefulness of MC in the rodent brain. The goal of the current work was to analyze and validate metabolic regional network alterations in three different mouse models of neurodegenerative diseases (β-amyloid and tau) by use of 2-deoxy-2-[^{18}F]fluoro-D-glucose positron emission tomography (FDG-PET) imaging. We compared the results of FDG-μPET MC with conventional VOI-based analysis and behavioral assessment in the Morris water maze (MWM). The impact of awake versus anesthesia conditions on MC read-outs was studied and the robustness of MC data deriving from different scanners was tested. MC proved to be an accurate and robust indicator of functional connectivity loss when sample sizes ≥12 were considered. MC readouts were robust across scanners and in awake/ anesthesia conditions. MC loss was observed throughout all brain regions in tauopathy mice, whereas β-amyloid indicated MC loss mainly in spatial learning areas and subcortical networks. This study established a methodological basis for the utilization of MC in different β-amyloid and tau mouse models. MC has the potential to serve as a read-out of pathological changes within neuronal networks in these models.

1. Introduction

In Alzheimer's disease (AD) the neurodegenerative process resulting in cognitive decline is characterized by structural and functional damage to the brain. Pathological alterations are characterized by regional atrophy in structural MRI (Barnes et al., 2009) and regional accumulation of pathological hallmarks such as extracellular β-amyloid and the intracellular deposition of hyperphosphorylated misfolded tau protein, which can be detected by PET imaging ligands. Several imaging modalities, including PET, can be used to visualize the neurodegenerative process in AD (Jack et al., 2016), such as hypometabolism in 2-deoxy-2-[^{18}F]fluoro-D-glucose positron emission tomography (FDG-PET) (Smailagic et al., 2015) and reduced functional connectivity in fMRI (Glover, 2011), as well as through a combination of those modalities (PET-MRI) (Judenhofer et al., 2008). FDG-PET allows to obtain not only single- or multi-region glucose uptake but also facilitates exploration of metabolic connectivity (MC) by consideration of the entire image pattern (Morbelli et al., 2012). Building on the clinical interpretation of FDG-PET imaging (Guedj et al., 2021), which is still considered one of the most informative biomarkers for dementia prediction in patients with mild cognitive impairment (MCI) (Morbelli et al., 2015), metabolic connectivity implies metabolic interactions of regional FDG uptake as a surrogate for cerebral energy consumption. Compared with classical FDG-PET data analysis, MC offers an additive value by capturing changes in relations between different brain regions and therefore allowing the investigation of functional metabolic

networks. For this reason, MC receives growing interest in AD research (Yakushev et al., 2017), and some studies applied the methodology also in preclinical settings (Zimmer et al., 2017; Grosch et al., 2021). However, the capability of MC to assess functional changes of inter- and intraregional network levels is still sparsely understood in mouse models of AD. Establishing MC in mouse models of neurodegenerative diseases could enable further exploration of model-specific neuronal network changes as well as serve as a valuable tool in the validation of biomarkers and therapeutics.

Therefore, this study aimed to interrogate the applicability of MC by analysis of interregion correlation coefficients (ICCs) in different β-amyloid and tau mouse models. Furthermore, we tested if MC has an additive value over a single region FDG-μPET analysis. We tested the robustness of the methodology by comparing standardized uptake value (SUV) and SUV ratio (SUVR) approaches for the assessment of MC and we questioned the required sample sizes by simulation analysis. Reproducibility of MC read-outs was validated by data comparison between μPET and μPET/MRI scanners as well as between mice injected in awake and anesthesia conditions. Finally, we compared MC and classical FDG quantification against spatial learning to test which read-out better reflects behavioral changes in β-amyloid and tau mouse models.

2. Materials and methods

2.1. Study design

All experiments were performed in compliance with the National Guidelines for Animal Protection, Germany, and with the approval of the regional animal committee (Regierung Oberbayern) and were overseen by a veterinarian. All animal experiments complied with the ARRIVE guidelines and were carried out in accordance with the U.K. Animals (Scientific Procedures) Act, 1986 and associated guidelines, EU Directive 2010/63/EU for animal experiments. Animals were housed in a temperature- and humidity-controlled environment with 12 h light-dark cycle, with free access to food (Sniff, Soest, Germany) and water. FDG-μPET data were collected from our in-house database for two different amyloid mouse models (PS2APP and APPPS1) and one tau-opathy mouse model (P301S) with age- and sex-matched wild-type (WT) controls (Table 1). All data were acquired in a highly standardized setting at LMU Munich between 2015 and 2021. FDG-μPET data were spatially co-registered to an FDG-μPET template. SUV and SUVR data were extracted using a set of predefined volumes of interest (VOIs) (Fig. 1). For SUVR calculation, scaling to the mean brain uptake was applied. Pearson's R were calculated as the index of regional ICC for SUV and SUVR approaches using the principle of Seed-Correlation (Yakushev et al., 2017) as an indicator for the connection strength of each VOI pair. A correlation matrix with all ICCs was created for every model. Average ICCs were calculated for the composite of functional regions (e.g.: all intra-neocortical connections (CTX-CTX) are represented in the Average ICC (CTX-CTX), which corresponds to the mean of all ICCs of cortical VOIs). After scans have been performed, mice were subject to a standardized Morris water maze (MWM) for behavioral testing. For APPPS1 we used different batches of mice for the scans and for behavioral testing at the group level, which, however, originated
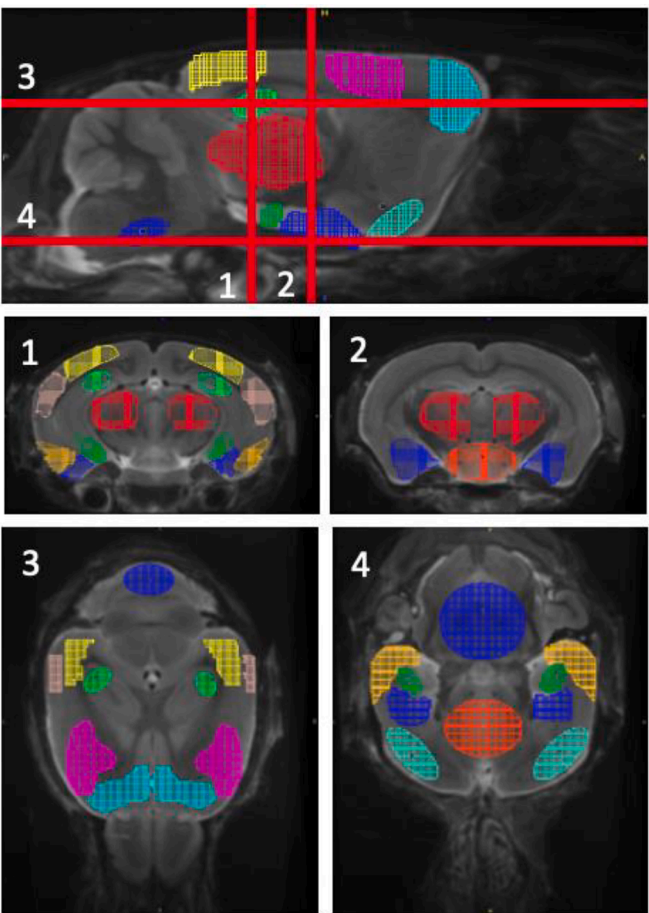
Table 1
Overview of FDG-μPET, μPET/MR and behavioral testing (MWM) data.

Mouse Strain	Age (months)	PET (n)	PET/MR (n)	MWM (n)
WT (Awake)	6.0	11	–	–
WT (Isoflurane)	6.0	11	–	–
PS2APP	8.6 ± 0.1	24	–	21
WT	7.8 ± 1.8	16	–	14
APPPS1	9.0 ± 3.0	16	12	8
WT	9.0 ± 3.0	25	17	8
P301S	6.3 ± 0.4	32	–	16
WT	6.0 ± 0.2	32	–	14

Fig. 1. Target regions used in the study projected on a mouse brain MRI atlas: bilateral cornu ammonis 1 (CA1) (light green) and 3 (CA3) (dark green), thalamus (red), amygdala (dark blue forebrain), entorhinal (light orange), piriform (turquoise), visual (yellow), auditory (pink), motor (light blue), somatosensory (purple) cortices as well as hypothalamus (orange), cerebellum (dark blue hindbrain) and brainstem (dark blue hindbrain).

from the same breeding line.

2.2. Animals

We analyzed FDG-μPET scans of PS2APP, APPPS1, and P301S mice together with age- and sex-matched wild-type (WT) controls. To test for an impact of anesthesia on metabolic connectivity in the mouse brain, we performed a head-to-head comparison between FDG injection in the awake state and during isoflurane anesthesia (6-month-old female WT mice). Here, eleven mice received two FDG-μPET scans with one week time gap. Awake and isoflurane conditions were switched between baseline and follow-up, starting with awake condition in 50 % of the sample.

PS2APP: The transgenic B6.PS2APP (line B6.152H) is homozygous for the human presenilin (PS) 2, N141I mutation, and the human amyloid precursor protein (APP) K670N, M671 L mutation (Weidensteiner et al., 2009). FDG-μPET scans in PS2APP ($n = 24$) were performed at 8.6 ± 0.1 months of age, and WT ($n = 16$) mice used for comparison were imaged at 7.8 ± 1.8 months of age.

APPPS1: The transgenic mouse line APPPS1 with the double mutation in APP and PSEN1 genes (APP KM670/671NL (Swedish), PSEN1 L166P) (Radde et al., 2006) express APP in the brain, driven by Thy1.2 promoter. FDG-μPET scans in APPPS1 ($n = 16$) and corresponding WT ($n = 25$) mice were conducted at 9.0 ± 3.0 months of age. FDG-μPET/MR scans in different APPPS1 mice ($n = 12$) were conducted

at 8.0 ± 2.7 months of age as well as in corresponding WT mice ($n = 17$) at 10.2 ± 2.3 months of age.

P301S: Homozygous human tau P301S mice comprise a mouse line expressing the human 0N4R tau isoform with the P301S mutation in exon 10 of the MAPT gene under the control of the murine thy1 promoter (Allen et al., 2002). FDG-μPET scans in P301S mice ($n = 32$) were conducted at 6.3 ± 0.4 months of age and in corresponding WT ($n = 32$) mice at 6.0 ± 0.2 months of age. There was no significant difference in age between transgenic and corresponding WT mice at the time of scanning (**Supplement Fig. 1**)

2.3. Radiochemistry and μPET recordings: data acquisition

[^{18}F]FDG was purchased commercially, and all μPET imaging was conducted as reported previously (Brendel et al., 2017). A minimal fasting period of four hours was kept before the PET scan. Before injection of 10.1 ± 2.1 MBq [^{18}F]FDG (in 150 μl saline), all mice were anesthetized with isoflurane (1.5 %, delivered at 3.5 L/min). Following tracer injection, animals were placed in the aperture of the Siemens Inveon DPET. Awake mice for the awake/anesthesia comparison, were placed directly in a restrainer, where tracer was rapidly injected (**Supplemental Fig. 2**). The uptake phase was up to 20 min in the awake state in a box. Anesthesia and placement in the μPET scanner occurred between 20 and 30 min after tracer injection. FDG injection was defined as time $t = 0$. For anesthesia mice, isoflurane was induced at $t = -10$ min before injection and the tail vein catheter was applied $t = -5$ min before injection. Isoflurane was continuously administered until $t = +30$ min after FDG-injection.

Static [^{18}F]FDG-PET emission recordings were made in an interval of 30–60 min after tracer injection, followed by a 15 min transmission scan using a rotating [^{57}Co] point source for attenuation correction (Brendel et al., 2017). Image reconstruction was performed using 3-dimensional ordered-subset expectation-maximization (4 iterations, 12 subsets) with 3-dimensional maximum a posteriori (32 iterations) (OSEM3D/MAP), a zoom factor of 1.0, and a voxel size of $0.78 \times 0.78 \times 0.8$ mm^3. Standard corrections for decay, scattered and random coincidences were performed.

A subset of APPPS1 mice from the same breeding line and at comparable age as well as matching WT mice were scanned with a 3T MedisonanoScan μPET/MR scanner (MedisoLtd, Hungary) with a single-mouse imaging chamber. A 15-minute anatomical T1 MR scan was performed 15 min after the [^{18}F]FDG injection (head receive coil, matrix size $96 \times 96 \times 22$, voxel size $0.24 \times 0.24 \times 0.8$ mm^3, repetition time 677 ms, echo time 28.56 ms, flip angle 90°). μPET acquisition was performed at 30–60 min post-injection. μPET data were reconstructed using a 3D iterative algorithm (Tera-Tomo 3D, MedisoLtd, Hungary) with the following parameters: matrix size $55 \times 62 \times 187$ mm^3, voxel size $0.3 \times 0.3 \times 0.3$ mm^3, 8 iterations, 6 subsets. Decay, random, and attenuation correction were applied. The T1 image was used to create a body-air material map for the attenuation correction.

2.4. μPET image analysis

Image registration was performed using PMOD Fusion tool (Version 3.5, PMOD Technologies, Basel, Switzerland) and consisted of two steps. First, individual FDG-μPET images were manually registered to a standard mouse T1w-MRI template in Ma-Benveniste-Mirrione space (Ma et al., 2005). Second, to cope for inter-individual differences in brain since and atrophy, FDG-μPET data were non-linearly registered to model-specific FDG-μPET templates based on intracerebral reference regions (Overhoff et al., 2016) using the automatic SPM5 procedure implemented in PMOD (equal modality, nonlinear warping with 16 iterations, a frequency cutoff of 3, a regularization of 1.0, no thresholding). All templates were located in a harmonized space with matching brain size. In particular, transformations were saved for each individual co-registered image to obtain a connected transformation

matrix from the native to the template space for each mouse brain. The connected transformation matrix was applied to the native space μPET data to guarantee minimal interpolation error.

As the μPET templates had been initially aligned to a single high-resolution T1 MR template, all final fused μPET images had the same spatial orientation and voxel dimensions, ($0.064 \times 0.064 \times 0.064$ mm^3) (Brendel et al., 2019). We conducted FDG-μPET intensity normalization of images to standardized uptake value (SUV) by conventional SUV calculation and to the whole brain global mean (SUVR; **Supplemental Fig. 3**). A VOI set based on functional compartments and networks in the rodent brain (Fig. 1) was designed for the extraction of regional FDG-μPET data. All VOIs were defined according to the Allen Mouse Brain Atlas and included: bilateral hippocampus CA1 (5 mm^3), hippocampus CA3 (7 mm^3), thalamus (26 mm^3), amygdala (12 mm^3), entorhinal cortex (10 mm^3), piriform cortex (9 mm^3), visual cortex (8 mm^3), auditory cortex (7 mm^3), motor cortex (20 mm^3) and somatosensory cortex (16 mm^3), as well as the hypothalamus (10 mm^3), cerebellum (12 mm^3) and brainstem (12 mm^3). The identical VOI set was used for all mouse models and corresponding WT.

2.5. Behavioral testing

PS2APP ($n = 21$), APPPS1 ($n = 8$), P301S ($n = 16$), and WT mice ($n = 22$) were investigated by an MWM test for spatial learning and motor deficits, which was performed according to a standard protocol (Sacher et al., 2019). On training days 1–5, each mouse had to perform four trials per day in the test basin, with the maximum time set to 70 s. The test trial was performed on day six. For analyses of escape latency and distance during MWM testing, we used the video tracking software Etho-Vision® XT 13 (Noldus). The frequency and velocity of reaching the platform were then determined from the recordings.

2.6. Statistics and calculations

All Statistical analyses were performed in SPSS (Version 26, IBM Deutschland GmbH, Ehningen, Germany) and GraphPad Prism 9 (GraphPad Prism 9.3.1 (350) Serial number: GPS-2,314,993).

Interregion correlation coefficients: SUV and SUVR data were tested for normal distribution with Kolmogorov-Smirnov tests. For each VOI pair, we calculated a Pearson's R correlation coefficient as an index of ICC. The ICCs were then visualized as heat maps (i.e. **Supplemental Fig. 4**). For regional data analysis, VOI pairs were assigned to functional entities, defined as average ICCs. Sets of identical ICCs were compared between groups by two-tailed paired t-tests, corrected for multiple comparisons using the Holm-Šídák method. A threshold of $p < 0.05$ was considered significant for the rejection of the null hypothesis.

Root mean square error and effect sizes: A simulation analysis was conducted to analyze appropriate cohort size and data robustness. A random number generator was used to reduce the cohort sizes by one mouse at a time, and a new ICC matrix was calculated for each cohort. For each sample size of P301S and matching sample size of WT controls, root mean square error (RMSE) was calculated (RMSE $= \sqrt{(\sum(\text{ICC}_{P301S} - \text{ICC}_{WT})^2 / n_{ICC})}$. Subsequently, the sample size-dependent effect size was calculated for individual regions using Cohen's d.

Inter-Scanner comparison: For the scanner comparison, Pearson's correlation coefficients (R) were calculated from the SUVR data of μPET and μPET/MR, respectively. These were used as index for the ICC from each VOI pair. The ICCs were plotted in heat maps and correlated with each other. A linear regression analysis and a paired t-test between the ICCs of both scanners were performed to assess quantitative agreement. In a subanalysis, the correlation between the intra-neocortical connections, as the most representative region, was also performed.

3. Results

3.1. SUVR scaling is more sensitive for the detection of MC differences between P301S and WT mice when compared to SUV

We used a large cohort of P301S and corresponding WT mice to run a simulation analysis to determine the effect of the sample size on MC results.

Smaller RMSE as a function of increased sample size was obtained for ICCs from SUV analysis (mean RMSE between $n = 10$–20: P301S $= 0.02 \pm 0.00$, WT $= 0.03 \pm 0.01$) when compared to ICCs derived from SUVR analysis (mean RMSE between $n = 10$–20: P301S $= 0.16 \pm 0.03$, WT $= 0.13 \pm 0.01$). For both approaches, RMSE was below 0.25 for a cohort size ≥ 12 mice (Fig. 2A).

ICCs derived from SUVR analysis delivered robust effect sizes for the contrast of MC quantification between P301S and WT mice when ≥ 12 mice were considered. Effect sizes for the P301S versus WT comparison of ICCs derived from SUV analysis were inferior when compared to ICCs derived from SUVR analysis, regardless of the sample size (Cohen's d [CTX-CTX]: AVG[SUVR] $= 0.40$; AVG[SUV] $= 0.06$; $p < 0.0001$; Fig. 2B). Overall, this analysis indicated that SUVR serve as a more sensitive read-out for MC alterations in P301S mice vs. WT mice.

3.2. [^{18}F]FDG SUVR and metabolic connectivity in awake and anesthetized mice are comparable

Previous studies have observed a reduction of cortical [^{18}F]FDG uptake in anesthetized rats, compared to awake animals at the time of [^{18}F]FDG injection (Shimoji et al., 2004). Such change in glucose uptake could lead to alterations of the metabolic pattern, which may lead to deviations in metabolic connectivity. For this purpose, we compared [^{18}F]FDG-μPET scans of WT mice after tracer injection in awake and anesthesia conditions.

Global mean normalized regional [^{18}F]FDG uptake was similar between awake injected mice and mice injected under isoflurane anesthesia in most of the studied VOIs (Fig. 3A and B). A reduced [^{18}F]FDG uptake was observed in the piriform cortex (SUVR[Awake] $= 1.04 \pm 0.07$; SUVR[Isofluran] $= 0.86 \pm 0.06$; $p < 0.0001$) in the anesthetized mice. In contrast, the hypothalamus (SUVR[Awake] $= 0.94 \pm 0.1$; SUVR[Isofluran] $= 1.09 \pm 0.04$; $p < 0.001$) and the amygdala (SUVR[Awake] $= 0.73 \pm 0.09$; SUVR[Isofluran] $= 0.82 \pm 0.05$; $p < 0.01$) showed significantly increased [^{18}F]FDG uptake in anesthesia condition (Fig. 3A). The correlation matrices show similar network patterns in awake and anesthesia conditions (Fig. 3C) and a strong overall correlation between the ICCs of the two matrices ($R = 0.77$; Fig. 3D). Direct

quantitative comparison of ICCs revealed no significant differences between both conditions (**Supplemental Fig. 5**)

3.3. Metabolic connectivity shows robust results for FDG-PET data derived from different scanners

For a reproducibility analysis, we performed the calculation of ICCs for APPPS1 β-amyloid and age-matched WT mice, with images acquired on two different μPET scanners (Siemens Inveon DPET; Mediso μPET/MRI) (Fig. 4). Based on SUVR data of both scanners, connectivity matrices showed a strong quantitative agreement when correlating all ICC for both APPPS1 mice and WT mice (R[APPPS1, all] $= 0.61$, $p < 0.0001$; R[WT, all] $= 0.62$, $p < 0.0001$) (**Supplemental Fig. 6**) as well as in a sub-analysis of only intra-neocortical connections (R[APPPS1, CTX-CTX] $= 0.67$, $p = 0.0001$; R[WT, CTX-CTX] $= 0.53$, $p = 0.0041$) (Fig. 4B). In the quantitative evaluation of intra-neocortical ICCs, no significant differences between μPET and μPET/MRI were evident for APPPS1 (ICC[CTX-CTX, μPET] $= 0.31 \pm 0.32$; ICC[CTX-CTX, μPET/MR] $= 0.29 \pm 0.40$; $p = 0.90$) or WT (ICC[CTX-CTX, μPET] $= 0.41 \pm 0.24$; ICC[CTX-CTX, μPET/MR] $= 0.42 \pm 0.27$; $p = 0.93$) (Fig. 4C).

3.4. ICCs indicate significant metabolic connectivity loss in β-amyloid and tau mouse models

PS2APP mice showed no significant difference compared to WT for intra-neocortical connections (ICC[CTX-CTX, PS2APP] $= 0.57 \pm 0.20$; ICC[CTX-CTX, WT] $= 0.54 \pm 0.23$; $p = 0.5$) (Fig. 5). Among regions of the spatial learning network, a loss of connections in PS2APP mice was found in the hippocampus (ICC[HIP, PS2APP] $= 0.33 \pm 0.21$; ICC[HIP, WT] $= 0.40 \pm 0.19$; $p = 0.001$) and the amygdala (ICC[AMY, PS2APP] $= 0.35 \pm 0.22$; ICC[AMY, WT] $= 0.53 \pm 0.22$; $p < 0.0001$). ICCs of brainstem connections did not indicate significant differences between this β-amyloid model and WT controls (ICC[BST, PS2APP] $= 0.45 \pm 0.23$; ICC[BST, WT] $= 0.42 \pm 0.22$; $p = 0.5$).

ICC Analysis in the APPPS1 model demonstrated no significant alterations in any network connections compared to WT controls besides from inter-cortical connections (ICC[SUBCTX-CTX, APPPS1] $= 0.29 \pm 0.19$; ICC[SUBCTX-CTX, WT] $= 0.36 \pm 0.21$; $p = 0.004$).

In P301S mice, ICCs for intra-neocortical connections showed a significantly lower connectivity compared to age and sex matched WT mice (ICC[CTX-CTX, P301S] $= 0.43 \pm 0.30$; ICC[CTX-CTX, WT] $= 0.54 \pm 0.23$; $p = 0.0012$). Among regions of the spatial learning network, there was a significant connectivity loss for hippocampal (ICC[HIP, P301S] $= 0.31 \pm 0.21$; ICC[HIP, WT] $= 0.40 \pm 0.19$; $p < 0.0001$) and amygdaloidal (ICC[AMY, P301S] $= 0.46 \pm 0.26$; ICC[AMY, WT] $= 0.57$
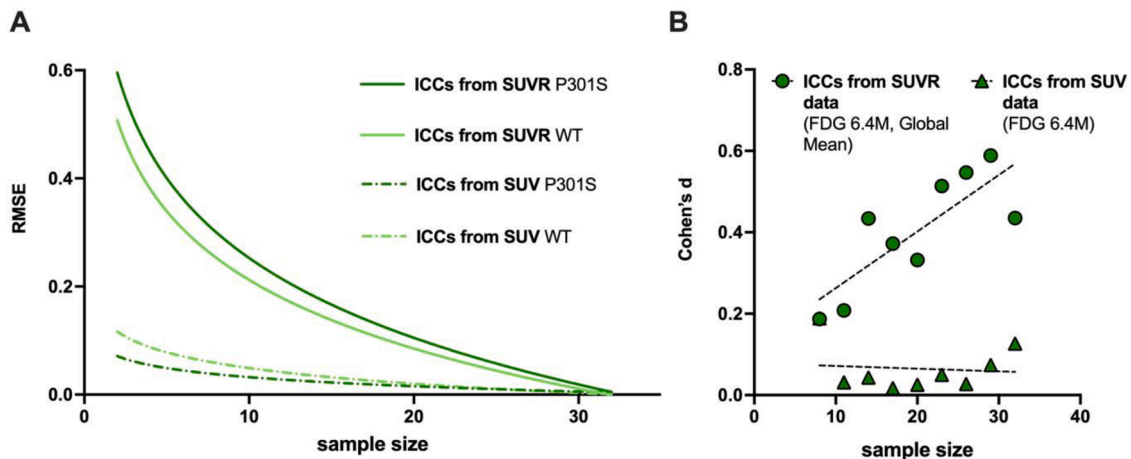
Fig. 2. A Root mean square error (RMSE) for ICCs derived from SUV and SUVR readouts according to sample size in P301S and WT controls. B Effect sizes (Cohens' d) in intra-neocortical connections (CTX-CTX) between P301S and WT controls for ICCs derived from SUV and SUVR readouts according to sample size.
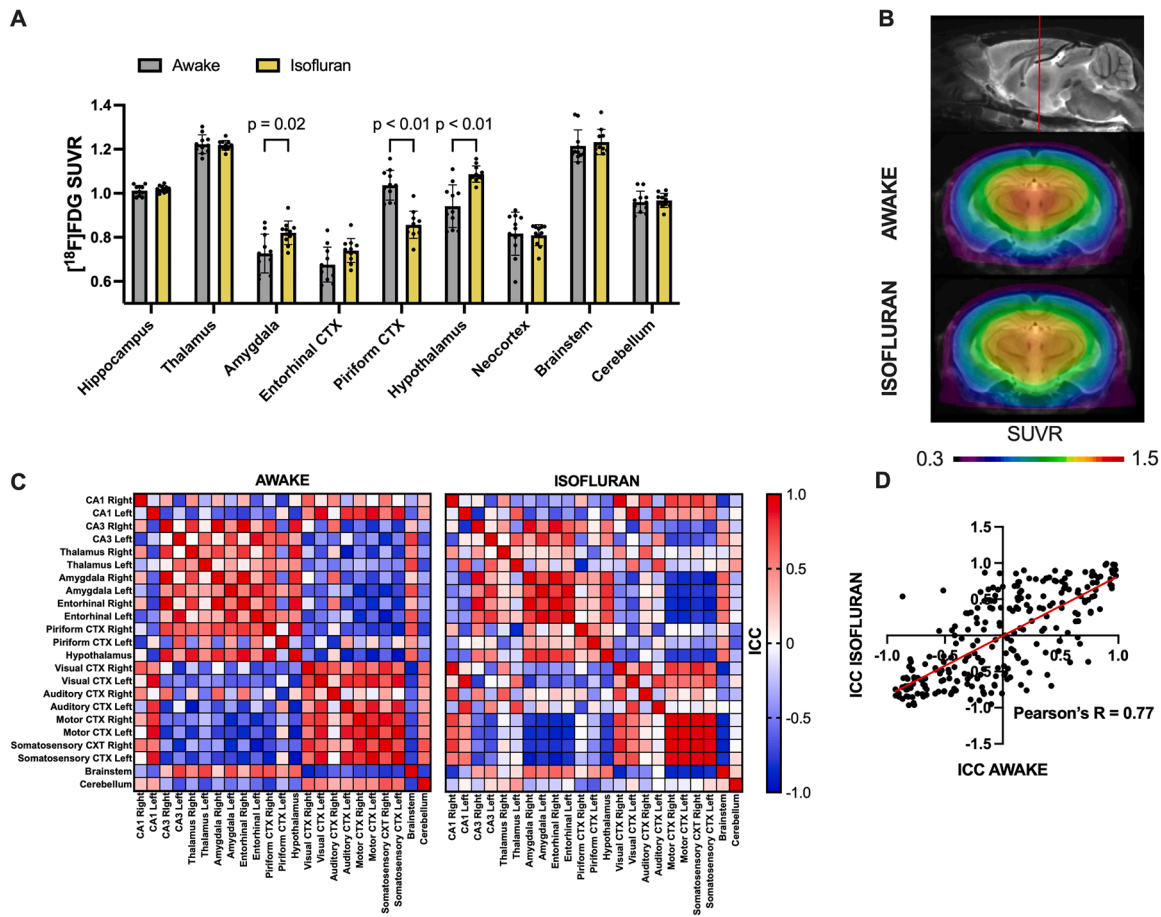
Fig. 3. A Global mean normalized [¹⁸F]FDG SUVR in the subgroups of awake and anesthetized wild-type mice; *$p < 0.05$; **$p < 0.01$; ***$p < 0.001$; ****$p < 0.0001$. B Group average images for wild-type mice injected awake and during anesthesia with isoflurane (global mean normalized). C Correlation matrix showing ICCs for all 23 analyzed brain regions in mice injected awake and during anesthesia. D Correlation plot between ICCs for all 23 analyzed brain regions in mice injected awake and during anesthesia.

± 0.19; $p = 0.018$) connections. Contrary to the amyloid models, connections of the brainstem did reveal a severe attenuation in P301S mice (ICC[BST, P301S] $= 0.25 ± 0.14$; ICC[BST, WT] $= 0.42 ± 0.22$; $p = 0.002$).

3.5. FDG-PET metabolic connectivity indicates better agreement with behavioral testing when compared to regional FDG uptake

Given the observed robust reductions of FDG-μPET MC in AD models, we questioned whether MC alterations may better resemble behavioral testing in AD mouse models when compared to common SUVR quantification of regional FDG uptake (Fig. 6). Escape latency in MWM was used as a surrogate of cognitive performance and velocity in MWM was used as a surrogate of the motor function.

VOI-based analysis of FDG-uptake in the area of motor function showed significant hypermetabolism in the PS2APP and APPPS1 model compared to WT (SUVR[MOT-CTX, PS2APP] $= 0.98 ± 0.05$; SUVR [MOT-CTX, WT] $= 0.87 ± 0.09$; $p < 0.0001$ / SUVR<[MOT-CTX, APPPS1] $= 0.94 ± 0.06$; SUVR[MOT-CTX, WT] $= 0.89 ± 0.06$; $p < 0.0001$. The tau model P301S revealed no significant difference in FDG-uptake of the motor cortex (SUVR[MOT-CTX, P301S] $= 0.83 ± 0.09$; SUVR[MOT-CTX, WT] $= 0.84 ± 0.10$; $p = 0.5$).

In contrast, MC analysis of connections between motor and remaining cortical VOIs revealed a significant loss of motor connections in P301S (ICCs[MOT-CTX, P301S] $= 0.29 ± 0.23$; ICCs[MOT-CTX, WT] $= 0.45 ± 0.17$; $p = 0.04$). However, no significant motor network alterations were observed in both mouse models of amyloidosis (ICCs

[MOT-CTX, PS2APP] $= 0.51 ± 0.2$; ICCs[MOT-CTX, WT] $= 0.55 ± 0.25$; $p = 0.61$ / ICCs[MOT-CTX, APPPS1] $= 0.22 ± 0.16$; ICCs[MOT-CTX, WT] $= 0.34 ± 0.2$; $p = 0.1$). An overview in differences in correlation matrices of all transgenic mouse models is provided in **Supplemental Fig. 7**. MC-based analysis was consistent with behavioral testing, where no significant velocity reduction was detected in PS2APP and APPPS1 mice (Velocity[AVG, PS2APP] $= 20$ cm/s ± 2 cm/s; Velocity[AVG, WT] $= 21$ cm/s ± 2 cm/s; $p = 0.35$ / Velocity[AVG, APPPS1] $= 19$ cm/s ± 4 cm/s; Velocity[AVG, WT] $= 19$ cm/s ± 1 cm/s; $p = 0.63$). A significant loss of motor function was measured in P301S mice (Velocity[AVG, P301S] $= 15$ cm/s ± 4 cm/s; Velocity[AVG, WT] $= 21$ cm/s ± 2 cm/s; $p < 0.0001$).

In brain regions associated with spatial learning, conventional VOI-based analysis of FDG-uptake showed no significant alterations in glucose metabolism in PS2APP and P301S mice (SUVR[HIP, PS2APP] $= 1.00 ± 0.05$; SUVR[HIP, WT] $= 1.01 ± 0.07$; $p = 0.16$ / SUVR[HIP, P301S] $= 1.00 ± 0.05$; SUVR[HIP, WT] $= 1.01 ± 0.06$; $p = 0.15$), but significant hypermetabolism in the β-amyloid model APPPS1 (SUVR [HIP, APPPS1] $= 1.00 ± 0.07$; SUVR[HIP, WT] $= 0.98 ± 0.04$; $p = 0.03$).

MC analysis based on ICCs of intra-subcortical connections detected significant connectivity loss in the PS2APP model (ICC[SUBCTX-SUBCTX, PS2APP] $= 0.32 ± 0.25$; ICC[SUBCTX-SUBCTX, WT] $= 0.41 ± 0.25$, $p = 0.013$) as well as in the P301S model (ICC[SUBCTX-SUBCTX, P301S] $= 0.33 ± 0.23$; ICC[SUBCTX-SUBCTX, WT] $= 0.41 ± 0.23$; $p = 0.005$; **Supplemental Fig. 7**). Thus, in the PS2APP and P301S models MC was in line with findings in behavioral testing, suggesting a loss of
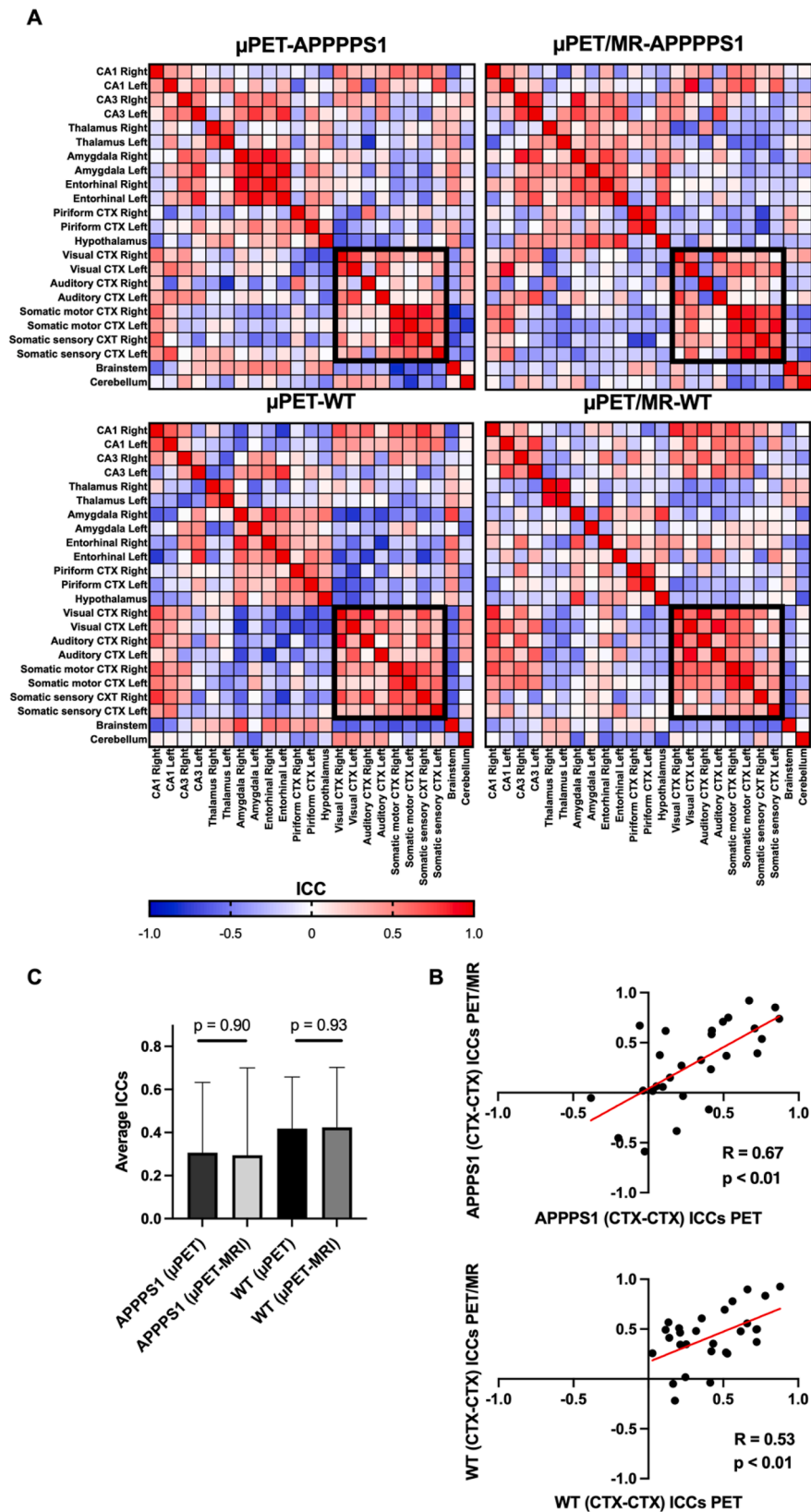
Fig. 4. Metabolic connectivity reproducibility analysis between dedicated μPET and μPET/MR scanners for APPPS1 and wild-type (WT) controls. A Correlation matrix of ICCs for all 23 VOIs and intra-neocortical connection (CTX-CTX) highlighted by the black frame. B Correlation of intra-neocortical ICCs (CTX-CTX) between μPET with μPET/MR, in APPPS1 and WT respectively. C Comparison of intra-neocortical ICCs between both scanners for APPPS1 and WT mice.
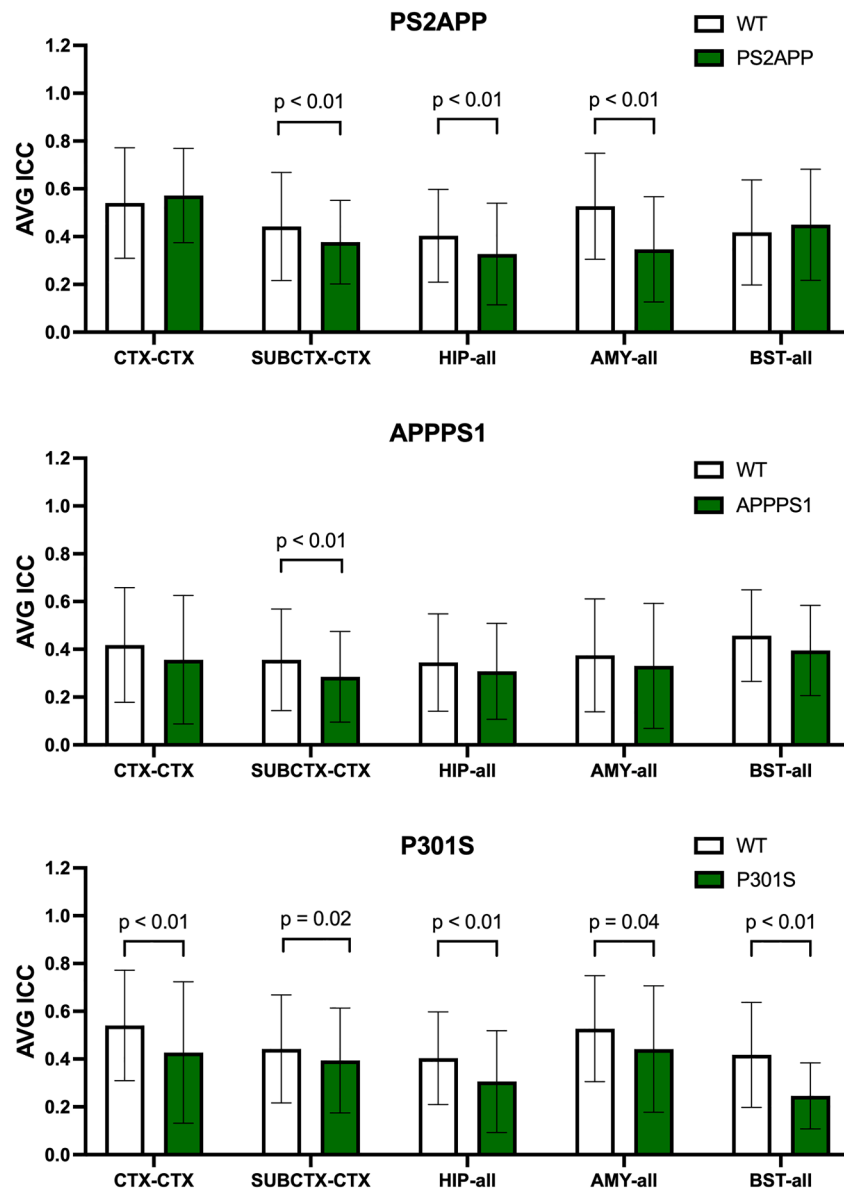
Fig. 5. Comparison of average ICC (AVG ICC) from μPET SUVR data in different transgenic (TG) mouse models versus corresponding wild-type (WT) controls in intra-neocortical (CTX-CTX), inter-cortical (SUBCTX-CTX), hippocampal (HIP-all), amygdaloidal (AMY-all) and brainstem (BST-all) connections; Multiple paired t tests corrected for multiple comparisons using the Holm-Šídák method (only comparisons with $p < 0.05$ are displayed).

spatial learning in MWM (Latency[AVG, PS2APP] $= 22\,s \pm 12\,s$; Latency [AVG, WT] $= 12\,s \pm 10\,s$; $p = 0.01$ / Latency[AVG, P301S] $= 37\,s \pm 20\,s$; Latency[AVG, WT] $= 12\,s \pm 10\,s$; $p < 0.001$). In the APPPS1 model no significant alterations of MC were observed (ICC[SUBCTX-SUBCTX, APPPS1] $= 0.31 \pm 0.25$; ICC[SUBCTX-SUBCTX, WT] $= 0.33 \pm 0.21$, $p = 0.56$), while significant loss of spatial memory (Latency[AVG, APPPS1] $= 42\,s \pm 21\,s$; Latency[AVG, WT] $= 22\,s \pm 12\,s$; $p = 0.046$) could be monitored.

4. Discussion

In this study, we performed a systematical analysis of MC in transgenic mouse models of neurodegenerative diseases using [18F]FDG-μPET. In Alzheimer's research, functional neuroimaging methods are of growing interest, as they allow the investigation of interacting brain regions and thus interregional network alterations. Among them, FDG-PET-based metabolic connectivity is increasingly used (Yakushev et al., 2017). Besides monitoring pathology-specific neuronal network

alterations and thus a more targeted evaluation of diagnostic and predictive value, utilization of MC in research of neurodegeneration also may enable assessment of functional changes in the brain during therapeutic intervention.

The informative value of MC has been proven in different clinical research studies, e.g. in a study demonstrating that the loss of connections, particularly to the posterior cingulate cortex (PCC), a region where hypometabolism is commonly associated with AD, precedes synaptic degeneration (Morbelli et al., 2012) and therefore proving a prediction value of MC on synaptic network alterations. Further hypometabolism in the PCC, as well as a decrease in metabolic correlation between PCC and the hippocampus, proved to be common to all AD subtypes, suggesting a functional decline in this connection as a core characteristic of AD (Herholz et al., 2018). Additionally, MC enables the analysis of specific neuronal networks, such as the dopaminergic mesocorticolimbic pathway on the issues of depression-typical network alterations in AD (Iaccarino et al., 2020).

Compared to clinical studies of humans, the usage of β-amyloid and
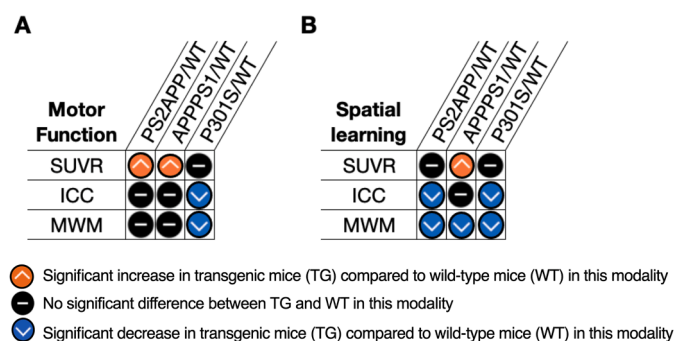
Fig. 6. Summary of significant differences ($p > 0.05$) between different transgene (TG) mouse models and matching wild-type (WT) for [¹⁸F]FDG-PET SUVR analysis, metabolic connectivity (MC) analysis and behavioral analysis (MWM). A Motor functions (SUVR = uptake in motor cortex VOIs; MC = average ICC in motor cortex connections, MWM = velocity). B Spatial learning (SUVR = uptake in hippocampal VOIs; MC = average ICC in intra-subcortical connections, MWM = escape latency).

tau mouse models allows for a more focused and individual analysis of pathological hallmarks of AD. However, MC has not widely been used for the investigation of neurodegeneration in transgenic mouse models of neurodegenerative diseases yet. MC has been established for the investigation of vestibular compensation in the rat brain after unilateral labyrinthectomy (Grosch et al., 2021), and in another rodent model, MC has been used to illustrate the neuroenergetic contribution of astrocytes in FDG-μPET of rat brains (Zimmer et al., 2017). In this study, we performed a systematical analysis of MC in β-amyloid and tau mouse models and thereby demonstrated the strengths and limitations of MC.

Most importantly, for all three investigated mouse models, the alterations in MC matched the phenotype in behavioral testing. The P301S tau model showed a robust MC decrease in networks associated with motor function as well as a significant loss in MC in spatial learning networks, which were in line with deficits in motor function and spatial learning. Contrary, a common SUVR-based FDG-μPET analysis was not sensitive enough to detect significant alterations of glucose uptake in these brain regions at the investigated age of 6.4 months in the cohort. In our previous study in tau P301S mice, we observed that early microglial inflammation was correlated with reduced cortical and hippocampal glucose uptake at the late stage (Eckenweber et al., 2020), regionally matching the seed regions of MC deficits. Tau-related impairments of glucose uptake and MC are also in line with a human AD study suggesting that elevated early tau is connected to decreased metabolism and reduced synaptic activity (Adams et al., 2019). In humans, tau spread through brain networks overlaps with a large range of functional networks. In contrast, the human β-amyloid network is characterized by a spatial pattern that shares large overlap with the default mode network (Sala et al., 2023). Correspondingly, our analysis of the tau mouse model showed a participation of all functional network units, reflected by the decrease in ICC whereas in β-amyloidosis models a decrease of cortical-subcortical connections can be found.

Interestingly, in both β-amyloidosis models PS2APP and APPPS1 where glial activation is linked to elevated relative glucose metabolism (Brendel et al., 2016; Xiang et al., 2021), MC showed likewise more coherent results with the MWM phenotype than VOI-based analyses. Conventional VOI-based analysis proved not sensitive or even showed contradictory results on network impairments for these models. According to our previous findings, we attribute this to increased microglial inflammation and thus increased glucose consumption in the β-amyloidosis mouse models, which must be considered in FDG-PET studies (Eckenweber et al., 2020). In APPPS1, amyloid-plaques appear in the cortex at 6 weeks of age and in the hippocampus at 3–4 months of age (Radde et al., 2006), much earlier than in PS2APP animals in which plaques are found at 6 months of age and a high plaque load is found in

the hippocampus at 10 months of age (Weidensteiner et al., 2009; Ozmen et al., 2009). In PS2APP microglial activation is age-dependent and correlates positively with the amyloid load (Brendel et al., 2016). Also in APPPS1, studies indicate, that microglial activation increases with aging and aggregates particularly within and around Aβ₄₂-positive plaques in the brain (Cao et al., 2021). Differences in the spatial arrangement and in the severity of microglial inflammation can be assumed between the two models, which also lead to differences in glucose metabolism.

In PS2APP mice, MC proved to be superior to a conventional analysis by showing clear network impairments in spatial learning regions, which cannot be monitored by a conventional VOI-based analysis. Moreover, in this model, MC served as a sensitive predictor for change in behavioral outcomes in MWM. In APPPS1 mice FDG-μPET data indicated a significant increase in hippocampal regions in the conventional VOI-based analysis, being completely contradictory to the significant loss of spatial learning functions we detected in the MWM at approximately 15 months of age, also confirmed by other behavioral studies (Webster et al., 2014). In contrast, using MC a minor decrease in hippocampal networks could be found. Although not significant this was still in better accordance with the findings of the behavioral testing, suggesting MC is less prone to microglial-inflammation-related change in FDG uptake. Furthermore, MC proved to be a more suitable predictor for motor functions and corresponding velocity in APPPS1 mice.

Regarding methodological aspects of the study, we considered SUVR scaling to be superior to an SUV scaling approach for the assessment of MC. Primarily measuring global heterogeneity an SUV-based scaling tends to be the less sensitive read-out of both. Large differences in regional cerebral uptake in individual mice lead to low basal correlations between different brain regions and thus consistently small effect sizes all derived from the utilization of SUV scaled data. Using a simulation analysis with a random number generator to evaluate the required sample size for the calculation of MC showed that SUVR scaling is the more stable and suitable readout. Effect sizes of SUVR scaled MC in intra-neocortical connections increased with each additional mouse and a sample size of approximately 12 mice was necessary to obtain significant effect sizes with a Cohen's d over 0.2 at a well acceptable RMSE <0.2. By performing a comparison of two different μPET scanners we could demonstrate scanner independent reproducibility of our data. Connectivity matrices showed similar patterns for both scanners, indicating data source independent applicability of MC for analysis of FDG-μPET scans.

In previous studies a difference in [¹⁸F]FDG uptake and regional distribution pattern between awake and isoflurane-anaesthetized rats was observed (Shimoji et al., 2004). In fact, differences in arterial blood flow and consecutive tracer distribution as well as cerebral glucose utilization can be argued. However, a specific study on [¹⁸F]FDG uptake in mice, showed similar values of whole brain [¹⁸F]FDG uptake in awake mice compared to isoflurane-anesthetized mice, supporting the routine use of isoflurane anesthesia in preclinical imaging studies (Bascunana et al., 2019). Likewise, we observed only minor impact of FDG injection during isoflurane anesthesia compared to awake injection in a head-to-head comparison. Regarding MC analyses, highly similar network connectivity between both conditions was observed. Therefore, we consider MC analyses of FDG-PET data in mice that was acquired after injection during isoflurane anesthesia to be valid and transferable to the awake state, which also supports the 3R principle of animal welfare.

Limitations that arose with the study of APPPS1 mice in the scanner comparison between μPET and μPET/MR, included a sample size disparity, due to different individual animals used in the scanner comparison, minor age differences between the groups (average 0.6 months for APPPS1 and 0.9 months for WT) as well as day-dependent difference in the test conditions which aggravated comparability as well as statistical accuracy. Additionally, the differences in the average images (**Supplemental Fig. 3**), ICCs (Fig. 4A and B), and R-values

(**Supplemental Fig. 6**) between the two scanners can be possibly explained by such inter-scanner differences as the reconstruction methods (μPET: OSEM3D/MAP; μPET/MR: Tera-Tomo), the images used for the attenuation correction (μPET: transmission scan; μPET/MR: MR scan), the spatial resolution (μPET: 1.5–3.0 mm FWHM in the radial direction and 1.5–1.8 mm FWHM in the tangential direction; μPET/MR: 1.50–2.01 mm FWHM and 1.32–1.65 mm, respectively; both reported for a point source and 2D filtered backprojection reconstruction), and the peak sensitivity (μPET: 11.1 %; μPET/MR: 8.4 %) (Visser et al., 2009; Nagy et al., 2013). Additional cross-scanner harmonization can be performed in the future to reduce the impact of these differences. However, in summary, we already observed a satisfactory agreement of MC read-outs derived from FDG-PET imaging of both machines, which likely represents a real-life scenario for pooling or comparing multi-center data.

Another limitation was the optimal VOI size for the calculation of MC in the mouse models used in the study. We did not apply VOIs for potential functional relevant subregions of several brain structures (i.e. thalamic nuclei) since the limited spatial resolution in μPET leads to an increase in statistical error with a smaller VOI size (Visser et al., 2009). Also, a potential proportionally larger spill in of bone uptake and stronger partial volume effects as well as increased cross-contamination of surrounding tissue due to atrophy might be a negative aspect of the usage of smaller cortical VOIs. Therefore, subsequent studies are desirable to determine the optimal VOI size for MC in mouse models. One more concern regarding MC in AD mouse models is the fact that MC is calculated at group level and therefore no conclusions can be drawn about individual mice. However in mouse models most important observations such as therapy effects of drugs are commonly made at group level. As preclinical usage of MC is sparse and to date no AD mouse studies have focused on monitoring of therapeutic effects using MC further research should be carried out in this promising field. Even though promising results were reported in this work, additional studies are needed to ensure the reproducibility of the applied methodology.

5. Conclusion

Our study proves that MC serves as a valid tool for the investigation of specific neuronal network changes in transgenic β-amyloid and tau mouse models. Compared with a conventional VOI-based μPET analysis MC shows higher agreement with results of behavioral testing in MWM as well as better detection of change of interregional glucose metabolism in different β-amyloid and tau mouse models. Functional connectivity studies in specific mouse models of neurodegenerative diseases could contribute to further insight into the link between pathology and brain function. Further MC may contribute to the validation of biomarkers and evaluation of disease-modifying therapeutics in AD.

Ethics statement

All animal experiments complied with the ARRIVE guidelines and were carried out in accordance with the U.K. Animals (Scientific Procedures) Act, 1986 and associated guidelines, EU Directive 2010/63/EU for animal experiments.

Disclosure

No potential conflicts of interest are reported for this study.

CRediT authorship contribution statement

François Ruch: Formal analysis, Writing – original draft, Investigation, Validation, Visualization, Methodology. **Johannes Gnörich:** Formal analysis, Investigation, Writing – review & editing. **Karin Wind:** Formal analysis, Investigation, Writing – review & editing. **Mara Köhler:** Formal analysis, Investigation, Writing – review & editing.

Artem Zatcepin: Investigation, Writing – review & editing. **Thomas Wiedemann:** Investigation, Writing – review & editing. **Franz-Joseph Gildehaus:** Investigation, Resources, Writing – review & editing. **Simon Lindner:** Investigation, Writing – review & editing. **Guido Boening:** Investigation, Resources, Writing – review & editing. **Barbara von Ungern-Sternberg:** Investigation, Writing – review & editing. **Leonie Beyer:** Conceptualization, Resources, Writing – review & editing. **Jochen Herms:** Conceptualization, Resources, Writing – review & editing. **Peter Bartenstein:** Conceptualization, Resources, Writing – review & editing. **Matthias Brendel:** Conceptualization, Formal analysis, Supervision, Writing – original draft, Funding acquisition, Writing – review & editing, Project administration. **Florian Eckenweber:** Conceptualization, Formal analysis, Supervision, Writing – original draft, Writing – review & editing, Project administration.

Declaration of competing interest

LB is an employee of Novartis. MB received speaker honoraria from GE healthcare, Roche and Life Molecular Imaging and is an advisor of Life Molecular Imaging. All other authors do not report a conflict of interest.

Data availability

Imaging data are available in nifti format and can be transferred per request by the corresponding author. Behavioral data and statistical analysis are available in table format on Mendeley Data. Statistics and Graphs are available per request as GraphPad Prism Data.

Acknowledgments

Supplementary materials

Supplementary material associated with this article can be found, in the online version, at doi:10.1016/j.neuroimage.2024.120513.

References

Adams, J.N., Lockhart, S.N., Li, L., Jagust, W.J, 2019. Relationships between tau and glucose metabolism reflect Alzheimer's disease pathology in cognitively normal older adults. Cereb. Cortex 29 (5), 1997–2009.

Allen, B., Ingram, E., Takao, M., Smith, M.J., Jakes, R., Virdee, K., et al., 2002. Abundant tau filaments and nonapoptotic neurodegeneration in transgenic mice expressing human P301S tau protein. J. Neurosci. 22 (21), 9340–9351.

Barnes, J., Bartlett, J.W., van de Pol, L.A., Loy, C.T., Scahill, R.I., Frost, C., et al., 2009. A meta-analysis of hippocampal atrophy rates in Alzheimer's disease. Neurobiol. Aging 30 (11), 1711–1723.

Bascunana, P., Thackeray, J.T., Bankstahl, M., Bengel, F.M., Bankstahl, J.P., 2019. Anesthesia and preconditioning induced changes in mouse brain [(18)F] FDG uptake and kinetics. Mol. Imaging Biol. 21 (6), 1089–1096.

Brendel, M., Probst, F., Jaworska, A., Overhoff, F., Korzhova, V., Albert, N.L., et al., 2016. Glial activation and glucose metabolism in a transgenic amyloid mouse model: a triple-tracer PET study. J. Nucl. Med. 57 (6), 954–960.

Brendel, M., Focke, C., Blume, T., Peters, F., Deussing, M., Probst, F., et al., 2017. Time courses of cortical glucose metabolism and microglial activity across the life span of wild-type mice: a PET study. J. Nucl. Med. 58 (12), 1984–1990.

Brendel, M., Deussing, M., Blume, T., Kaiser, L., Probst, F., Overhoff, F., et al., 2019. Late-stage Anle138b treatment ameliorates tau pathology and metabolic decline in a mouse model of human Alzheimer's disease tau. Alzheimers Res. Ther. 11 (1), 67.

Cao, S., Fisher, D.W., Rodriguez, G., Yu, T., Dong, H., 2021. Comparisons of neuroinflammation, microglial activation, and degeneration of the locus coeruleus-norepinephrine system in APP/PS1 and aging mice. J. Neuroinflamm. 18 (1), 10.

Eckenweber, F., Medina-Luque, J., Blume, T., Sacher, C., Biechele, G., Wind, K., et al., 2020. Longitudinal TSPO expression in tau transgenic P301S mice predicts increased tau accumulation and deteriorated spatial learning. J. Neuroinflamm. 17 (1), 208.

Glover, G.H., 2011. Overview of functional magnetic resonance imaging. Neurosurg. Clin. N. Am. 22 (2), 133–139 vii.

Grosch, M., Lindner, M., Bartenstein, P., Brandt, T., Dieterich, M., Ziegler, S., et al., 2021. Dynamic whole-brain metabolic connectivity during vestibular compensation in the rat. Neuroimage 226, 117588.

Guedj, E., Varrone, A., Boellaard, R., Albert, N.L., Barthel, H., van Berckel, B., et al., 2021. EANM procedure guidelines for brain PET imaging using [(18)F]FDG, version 3. Eur. J. Nucl. Med. Mol. Imaging.

Herholz, K., Haense, C., Gerhard, A., Jones, M., Anton-Rodriguez, J., Segobin, S., et al., 2018. Metabolic regional and network changes in Alzheimer's disease subtypes. J. Cereb. Blood Flow Metab. 38 (10), 1796–1806.

Iaccarino, L., Sala, A., Caminiti, S.P., Presotto, L., Perani, D., 2020. Alzheimer's disease neuroimaging I. *In vivo* MRI structural and PET metabolic connectivity study of dopamine pathways in Alzheimer's disease. J. Alzheimers Dis. 75 (3), 1003–1016.

Jack, C.R., Bennett, D.A., Blennow, K., Carrillo, M.C., Feldman, H.H., Frisoni, G.B., et al., 2016. A/T/N: an unbiased descriptive classification scheme for Alzheimer disease biomarkers. Neurology 87 (5), 539–547.

Judenhofer, M.S., Wehrl, H.F., Newport, D.F., Catana, C., Siegel, S.B., Becker, M., et al., 2008. Simultaneous PET-MRI: a new approach for functional and morphological imaging. Nat. Med. 14 (4), 459–465.

Ma, Y., Hof, P.R., Grant, S.C., Blackband, S.J., Bennett, R., Slatest, L., et al., 2005. A three-dimensional digital atlas database of the adult C57BL/6J mouse brain by magnetic resonance microscopy. Neuroscience 135 (4), 1203–1215.

Morbelli, S., Drzezga, A., Perneczky, R., Frisoni, G.B., Caroli, A., van Berckel, B.N., et al., 2012. Resting metabolic connectivity in prodromal Alzheimer's disease. A European Alzheimer disease consortium (EADC) project. Neurobiol. Aging 33 (11), 2533–2550.

Morbelli, S., Garibotto, V., Van De Giessen, E., Arbizu, J., Chetelat, G., Drezgza, A., et al., 2015. A cochrane review on brain [(1)(8)F]FDG PET in dementia: limitations and future perspectives. Eur. J. Nucl. Med. Mol. Imaging 42 (10), 1487–1491.

Nagy, K., Toth, M., Major, P., Patay, G., Egri, G., Haggkvist, J., et al., 2013. Performance evaluation of the small-animal nanoScan PET/MRI system. J. Nucl. Med. 54 (10), 1825–1832.

Overhoff, F., Brendel, M., Jaworska, A., Korzhova, V., Delker, A., Probst, F., et al., 2016. Automated spatial brain normalization and hindbrain white matter reference tissue give improved [(18)F]-florbetaben PET quantitation in Alzheimer's model mice. Front. Neurosci. 10, 45.

Ozmen, L., Albientz, A., Czech, C., Jacobsen, H., 2009. Expression of transgenic APP mRNA is the key determinant for beta-amyloid deposition in PS2APP transgenic mice. Neurodegener. Dis. 6 (1–2), 29–36.

Radde, R., Bolmont, T., Kaeser, S.A., Coomaraswamy, J., Lindau, D., Stoltze, L., et al., 2006. Abeta42-driven cerebral amyloidosis in transgenic mice reveals early and robust pathology. EMBO Rep. 7 (9), 940–946.

Sacher, C., Blume, T., Beyer, L., Peters, F., Eckenweber, F., Sgobio, C., et al., 2019. Longitudinal PET monitoring of amyloidosis and microglial activation in a second-generation amyloid-beta mouse model. J. Nucl. Med. 60 (12), 1787–1793.

Sala, A., Lizarraga, A., Caminiti, S.P., Calhoun, V.D., Eickhoff, S.B., Habeck, C., et al., 2023. Brain connectomics: time for a molecular imaging perspective? Trends Cogn. Sci. 27 (4), 353–366.

Shimoji, K., Ravasi, L., Schmidt, K., Soto-Montenegro, M.L., Esaki, T., Seidel, J., et al., 2004. Measurement of cerebral glucose metabolic rates in the anesthetized rat by dynamic scanning with 18F-FDG, the ATLAS small animal PET scanner, and arterial blood sampling. J. Nucl. Med. 45 (4), 665–672.

Smailagic, N., Vacante, M., Hyde, C., Martin, S., Ukoumunne, O., Sachpekidis, C., 2015. (1)(8)F-FDG PET for the early diagnosis of Alzheimer's disease dementia and other dementias in people with mild cognitive impairment (MCI). Cochrane Database Syst. Rev. 1, CD010632.

Visser, E.P., Disselhorst, J.A., Brom, M., Laverman, P., Gotthardt, M., Oyen, W.J., et al., 2009. Spatial resolution and sensitivity of the Inveon small-animal PET scanner. J. Nucl. Med. 50 (1), 139–147.

Webster, S.J., Bachstetter, A.D., Nelson, P.T., Schmitt, F.A., Van Eldik, L.J., 2014. Using mice to model Alzheimer's dementia: an overview of the clinical disease and the preclinical behavioral changes in 10 mouse models. Front. Genet. 5, 88.

Weidensteiner, C., Metzger, F., Bruns, A., Bohrmann, B., Kuennecke, B., von Kienlin, M., 2009. Cortical hypoperfusion in the B6.PS2APP mouse model for Alzheimer's disease: comprehensive phenotyping of vascular and tissular parameters by MRI. Magn. Reson. Med. 62 (1), 35–45.

Xiang, X., Wind, K., Wiedemann, T., Blume, T., Shi, Y., Briel, N., et al., 2021. Microglial activation states drive glucose uptake and FDG-PET alterations in neurodegenerative diseases. Sci. Transl. Med. 13 (615), eabe5640.

Yakushev, I., Drzezga, A., Habeck, C., 2017. Metabolic connectivity: methods and applications. Curr. Opin. Neurol. 30 (6), 677–685.

Zimmer, E.R., Parent, M.J., Souza, D.G., Leuzy, A., Lecrux, C., Kim, H.I., et al., 2017. [(18)F]FDG PET signal is driven by astroglial glutamate transport. Nat. Neurosci. 20 (3), 393–395.